ACS OMEGA

http://pubs.acs.org/journal/acsodf

Article

Gas–Liquid Flow Pattern and Hydrate Risk in Wellbore during the Deep-Water Gas-Well Cleanup Process

Dayong Chen and Zheng Sun*

Cite This: *ACS Omega* 2023, 8, 12911–12921

Read Online

ACCESS | Metrics & More | Article Recommendations

ABSTRACT: The wellbore fluid flow characteristics and hydrate flow assurance problems during the deep-water gas well cleanup process seriously affect the safety of gas well testing. Aiming at the process of deep-water gas well cleanup where the liquid gas ratio changes dramatically, this study reveals the distribution law of gas–liquid flow patterns in the wellbore. Combined with the clean test conditions of deep-water gas wells, the transient numerical simulation and analysis are carried out. At the same time, a hydrate risk prediction model suitable for the well cleanup process is established to predict the hydrate risk under different cleaning conditions. The research results are as follows: (1) after flowback, the temperature at the wellhead and mud line presents different characteristics of temperature change, the wellhead temperature decreases first and then increases, while the flow temperature at the mud line rises first and then decreases; (2) slug flow and annular flow are more likely to occur in the wellbore under low wellhead pressure. Bubble flow often appears in the initial stage of flowback under high wellhead pressure and gradually changes into slug and annular flow patterns in the middle and late stages; (3) at the same flowback time, the wellbore will also present different flow patterns along the way. The lower part of the well bore mainly presents bubble flow and slug flow, and the upper and middle parts of the well bore mainly present annular flow patterns; (4) high liquid–gas ratio conditions, proper well cleaning speed, and the use of hydrate inhibitors can effectively reduce the hydrate risk during the cleaning process of deep-water gas wells.

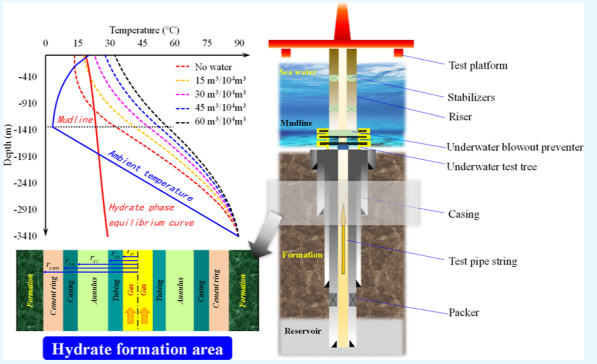

1. INTRODUCTION

The completion test of deep-water gas wells is an important link to obtain formation reservoir parameters and evaluate the development potential of gas reservoirs. It is also a "temporary step" for deep-water gas wells to be put into production.[1−3] As the deep-water testing conditions are severe and the fluid temperature and pressure are variable, the test string usually has conditions for hydrate formation. The pipe string shrinkage caused by hydrate formation and deposition will pose an obstacle to the test flow, that is, the hydrate flow obstacle.[4−6] At present, the formation of hydrate flow barrier has become one of the most serious flow assurance problems in the process of deep-water gas well testing, which has an irreversible impact on testing. Deep-water gas well cleanup is the process of liquid flowback in the wellbore and near the well before production test. The flowback fluid is usually a mixture of multiple fluids, including reservoir produced fluid, test fluid, induced fluid pad, and annular drilling fluid. The blowout cleaning process is multiphase unsteady flow of flowback liquid and produced gas in the wellbore. The liquid gas ratio is significantly higher than other test conditions, and the gas–liquid flow pattern is more variable. Clarifying the flow characteristics of gas–liquid fluid in the wellbore during well cleanup stage is very important for studying the safety guarantee of deep-water wellbore flow and ensuring the gas well testing safety.[7−10]

At present, the hydrate phase equilibrium conditions are mainly determined by empirical graphic method, phase equilibrium constant method and statistical thermodynamics method. Among them, statistical thermodynamic method is the most accurate and commonly used calculation method. Since the 1950s, experts and scholars around the world have carried out a lot of scientific research on the thermodynamic equilibrium theory of hydrate. In 1959, based on the hydrate unit cell model and Langmuir gas isotherm adsorption theory, Van der Waals and Platteeuw (1959) derived the hydrate phase equilibrium model using classical statistical thermodynamic methods,[11] which became the basis of most subsequent hydrate statistical thermodynamic models. Since the VdW-P model is mostly applicable to single-phase gas, Parrish and

Received: January 5, 2023
Accepted: March 20, 2023
Published: March 29, 2023

Prausnitz (1972) calculated Langmuir parameters as temperature functions through empirical expressions,[12] and proposed a calculation model for hydrate phase equilibrium conditions applicable to multi-component mixed gas. This model is more practical and widely used. In 1976, Ng and Robinson (1976) considered the interaction between guest molecules,[13] modified the Langmuir constant in VdW-P model, and established a modified hydrate phase equilibrium calculation model, which has a high prediction accuracy for hydrate formation conditions in the gas liquid hydrate region. In 1985, Holder and John (1985) used the three-layer sphere model to describe the interaction between guest molecules and water molecules,[14] taking into account the influence of spherical asymmetry effect of actual gas molecules, the deviation between Langmuir constant and ideal value, and so forth, and proposed an improved equation of state for hydrate phase equilibrium. Different from the VdW-P model, in 1996, Chen and Guo et al. (1966, 1998) based on the kinetic mechanism of hydrate formation and considering the non-stoichiometry of hydrate formation,[15,16] deduced the fugacity formula of guest molecules using statistical thermodynamics, and established a new prediction model for hydrate phase equilibrium conditions, which has improved the prediction accuracy compared with the VdW-P model.[17,18] In 2000, Javanmardi and Moshfeghian (2000) proposed a hydrate phase equilibrium prediction method without flash calculation based on the Parrish Prausnitz model.[19] This model has a wide range of applications and can accurately predict the formation conditions of gas hydrate in one or more electrolyte solutions.

In view of the deep-water gas well testing process, some researchers have conducted prediction research on the hydrate flow obstacles in the test wellbore. In 2001, Reyna and Stewart (1959) described a deep-water test process.[20] During the test of deep-water gas wells, it was suddenly found that hydrate was formed in the tubing string in the riser above the mud line, and the test process was stopped. The production diagnostic test found that the initial blockage was caused by wax deposition and hydrate formation. Finally, it was solved by injecting ethylene glycol and seawater through coiled tubing. In 2011, Arrieta et al. (2011)[21] took an ultra-deep-water gas well in Mexico as an example to analyze the formation conditions and process of hydrate flow barriers during deep-water gas well testing. As well as the importance of flow barrier prevention, they put forward guidance and suggestions on the use of coiled tubing, hydrate inhibitor injection, and well cleaning process. Wang Zhiyuan et al. (2018; 2019a; and 2019b) put forward a prediction method for the formation area of natural gas hydrate in the wellbore during deep-water gas well testing.[22−24] They analyzed the sensitivity of gas production, gas composition, geothermal gradient, water depth, inhibitor content, and other parameters during testing to the impact of wellbore hydrate risk area. From 2018 to 2020, Yang et al. (2019a; 2019b) and Liu et al. (2018) established a prediction model for hydrate deposition and plugging in the wellbore.[25−27] They proposed that the hydrate deposition layer on the inner wall of the wellbore presents uneven thickness during deep-water gas well testing, which is related to the test conditions of the existence of free water, and predicted the location and hydrate deposition in the wellbore where hydrate plugging is most likely to occur.

At present, researchers mainly use the temperature and pressure calculation model to obtain the temperature and pressure distribution along the deep-water wellbore. For the well cleanup process where the liquid gas ratio changes dramatically, it is not easy to obtain accurate wellbore temperature and pressure change rules, and it is difficult to describe the distribution and change characteristics of gas−liquid flow patterns. To solve above problems, on the basis of analyzing the cleanup conditions of deep-water gas wells, the transient multiphase flow simulation software OLGA was innovatively used for the first time to carry out the transient numerical simulation of well cleaning,[28−30] which revealed the characteristics of wellbore gas−liquid flow during the well cleanup stage. At the same time, a hydrate prediction model was established for the well cleaning process, which predicted the hydrate formation risk in the wellbore under different well cleanup conditions, it provides theoretical guidance for the research on deep-water wellbore flow assurance.

2. WELL CLEANUP PROCESS OF DEEP-WATER GAS WELL

Gas reservoir productivity testing methods generally include back pressure well testing, isochronous well testing, and improved isochronous well testing. At present, for the "one on and one off" conventional back-pressure test commonly used in deep-water gas wells, the test process can be divided into three stages.

(1) During the well cleaning and flowback stage, the drilling fluid and completion fluid and formation fluid in the wellbore and near the well will be returned to the ground, so that the gas well can meet the requirements for entering the production stage and meet the conditions for opening the gas well;

(2) In the variable production test stage, representative oil and gas samples are obtained, and the formation pressure change data in the production process is obtained as required to establish the productivity equation;

(3) In the shut-in pressure recovery stage, the formation pressure recovery data were obtained and the reservoir parameters were solved.

The well bore schematic diagram of the deep-water well cleanup process is shown in Figure 1. Before the oil and gas well is put into production, the fluid near the wellbore and formation shall be cleaned through flowback, and relevant data of oil and gas reservoir development shall be obtained to prepare for subsequent production.

The well cleanup process has important purposes and functions: (1) return the drilling fluid, completion fluid, and formation fluid in the wellbore to the surface; (2) obtain fluid analysis data; and (3) obtain formation pressure data and shut-in pressure recovery data during well opening, and obtain representative surface PVT oil and gas samples and surface conventional oil and gas samples.

3. TRANSIENT NUMERICAL SIMULATION OF WELL CLEANUP PROCESS

In this study, the cleanup process of a deep-water gas well is simulated. The key parameters include the following: completion fluid volume 1380 m^3; completion fluid density 1.3 g/cm^3; maximum flowback volume 60×10^4 m^3/d; and well cleaning time is 12 h. The observation point is set at the wellhead and mud line. The other basic parameters and natural gas composition of deep-water gas wells are shown in Tables 1

https://doi.org/10.1021/acsomega.3c00074
ACS Omega 2023, 8, 12911−12921

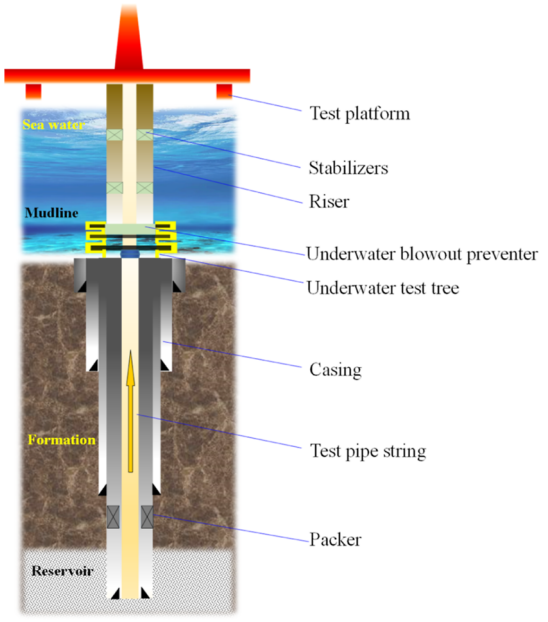

Figure 1. Wellbore structure of deep-water gas well for the well cleanup process.

and 2, respectively. The related constant parameters for calculation are shown in Table 3.

Table 1. Basic Parameters of Deep-Water Gas Well (X Well)

parameter	unit	value
formation depth	m	3410
water depth	m	1350
reservoir pressure	MPa	39.5
reservoir temperature	°C	89.5
pressure gradient	MPa/100 m	1.2
geothermal gradient	°C/100 m	3.87
seawater surface temperature	°C	20
mud line temperature	°C	3.2
test gas volume	10^4 m^3/d	10 ~ 150
test string diameter	in	5−1/2
riser diameter	in	21
casing diameter	in	≥9−8/5

The temperature and pressure distribution along the wellbore and fluid flow characteristics under different blowout volumes and wellhead blowout pressures are simulated, and the fluid flow diagram is shown in Figure 2.

3.1. Effect of Flowback Volume. The simulation results show that the liquid flowback volumes are 20 × 10^4, 50 × 10^4, and 80 × 10^4 m^3/d. The change of temperature and liquid holdup at the wellhead and the change of pressure and temperature at the mud line are shown in Figure 3.

It can be seen from Figure 3a that the initial temperature of the wellhead is equal to the sea level temperature (20 °C). Since the initial temperature of the liquid column along the wellbore is the same as the ambient temperature outside the pipe, the temperature at the wellhead decreases due to the rising flow of fluid near the mud line, and then, the temperature rises due to the flow of high-temperature fluid below the mud line. Later, when the liquid column is basically returned, the fluid flow in the wellbore tends to be stable, the wellhead temperature also becomes gentle.

It can be seen from Figure 3b that with the discharge of the liquid in the wellbore, the liquid holdup at the wellhead gradually decreases from ″1″ to near the value of ″0″. The significant drop in the liquid holdup indicates that the liquid phase in the wellbore is basically drained, and the residual liquid phase in the later stage is from the formation produced water or gas phase condensate water. It can be seen that with the increase of venting amount, the time for liquid main body to be discharged is obviously shortened, and the venting amounts are 20 × 10^4, 50 × 10^4, and 80 × 10^4 m^3/d. The liquid phase discharge times are 3300, 2000, and 1400 s, respectively.

Table 3. Related Constant Parameters for Calculation

parameter	unit	value
average molar mass of natural gas	kg·mol−1	0.0179
molar mass of aqueous phase	kg·mol−1	0.018
molar density of natural gas in hydrate phase	mol·m−3	7540
density of aqueous phase	mol·m−3	998
density of hydrate phase	mol·m−3	950
enthalpy of hydrate formation	J·kg−1	6.4 × 10^5
activation temperature for hydrate formation	K	1.36 × 10^4
interfacial tension between hydrocarbon and water	N·m−^{1}	0.072
kinetic constant for hydrate formation	dimensionless	3.632
empirical coefficient for hydrate formation	dimensionless	0.85
roughness of pipeline inner wall	m	4.2 × 10^{-5}
thermal conductivity of hydrate layer	W·(m·K)$^{-1}$	0.45
thermal conductivity of test string	W·(m·K)$^{-1}$	52.5
thermal conductivity of casing string	W·(m·K)$^{-1}$	52.5
thermal conductivity of cement ring	W·(m·K)$^{-1}$	0.45
thermal conductivity of formation	W·(m·K)$^{-1}$	1.7
convection heat transfer coefficient	W·(m·K)$^{-1}$	1050

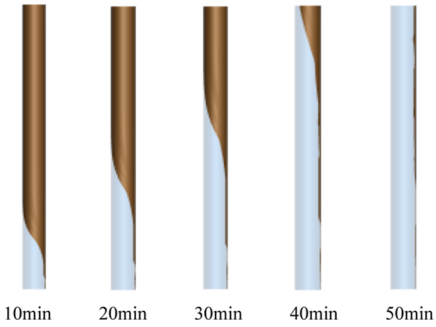

Figure 2. Schematic diagram of fluid flow simulation in wellbore during the well cleanup process.

Table 2. Basic Parameters of Natural Gas

gas composition (%)										
CH_4	C_2H_6	C_3H_8	*i*-C_4H10	*n*-C_4H_{10}	*i*-C_5H_{12}	C_6^+	N_2	CO_2	relative molar mass	relative density
88	5.4	0.56	0.3	0.45	0.13	0.1	2.1	1.85	17.9	0.617

https://doi.org/10.1021/acsomega.3c00074
ACS Omega 2023, 8, 12911−12921

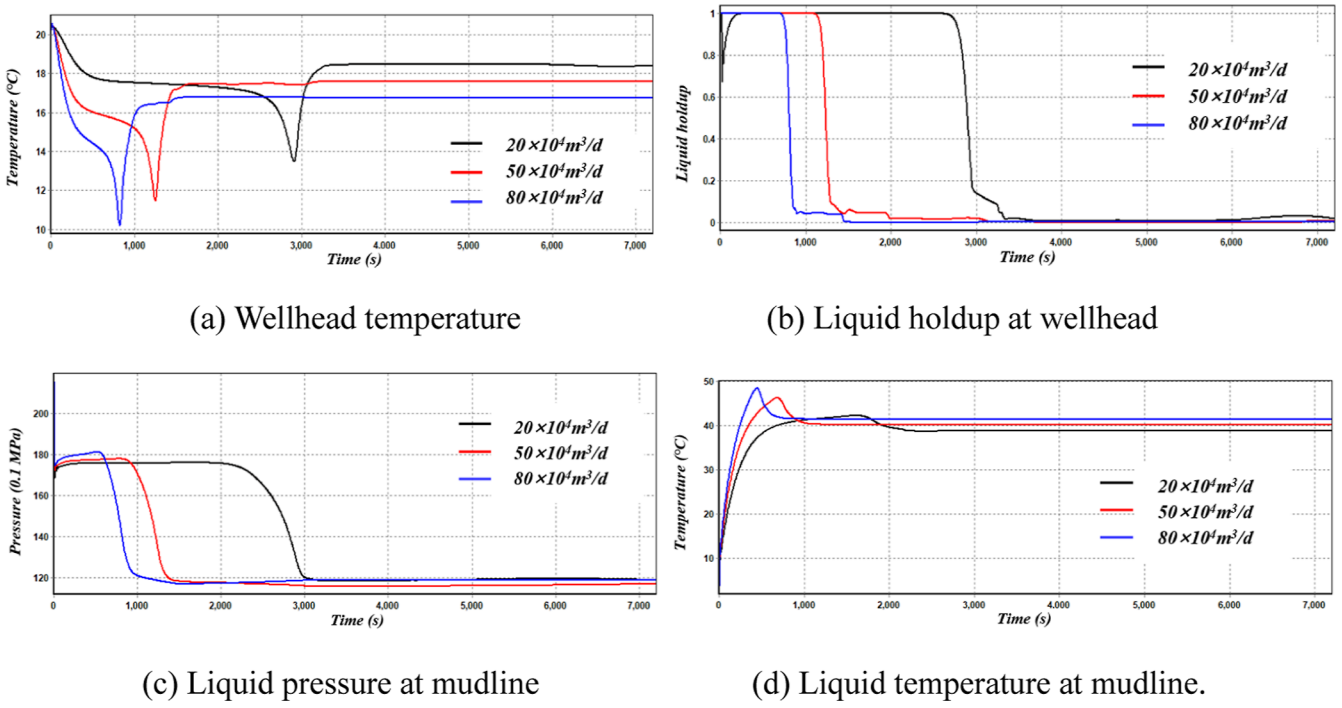

(a) Wellhead temperature (b) Liquid holdup at wellhead

(c) Liquid pressure at mudline (d) Liquid temperature at mudline.

Figure 3. Effect of gas release volume on fluid flow in wellbore.

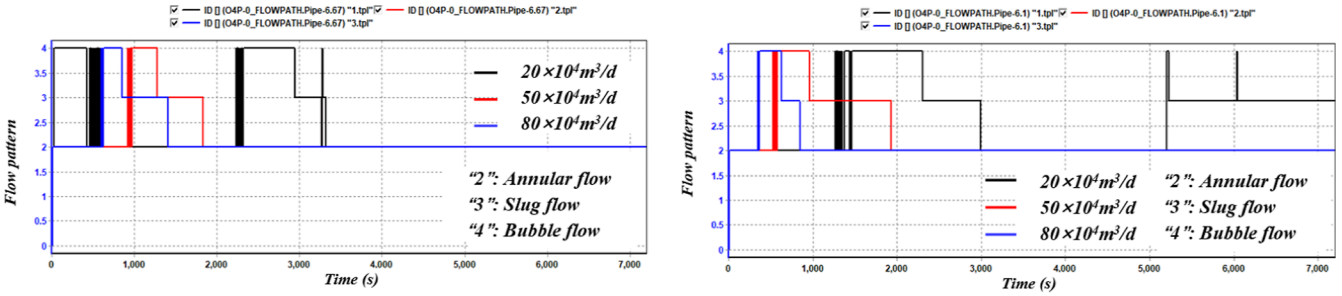

(a) The change of flow pattern at wellhead (b) The change of flow pattern at mudline

Figure 4. Change of liquid holdup at the mud line.

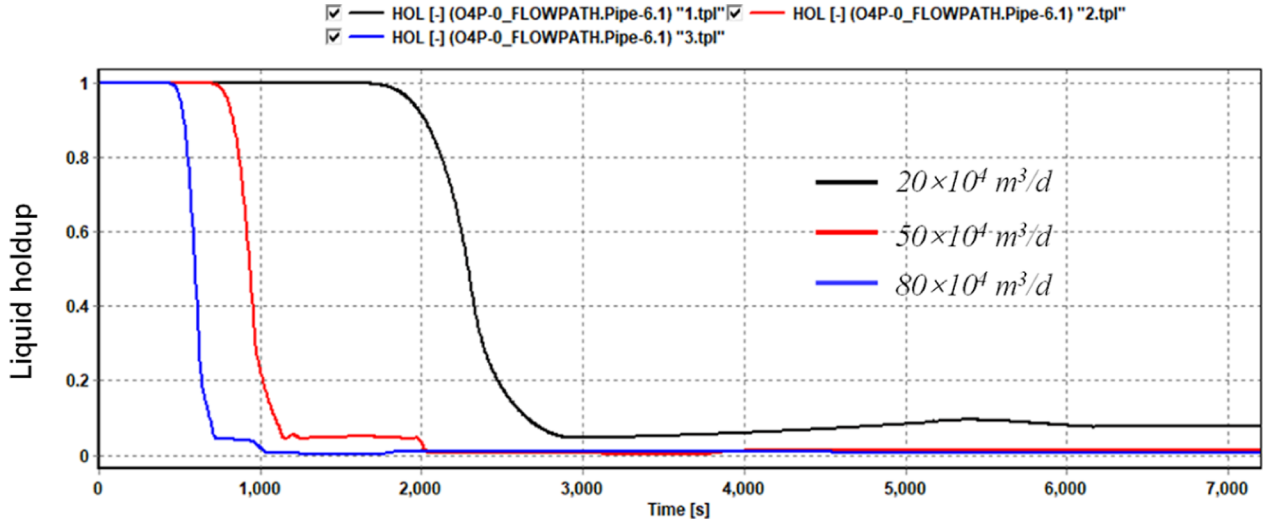

Figure 5. Influence of gas release rate on the flow pattern in the wellbore.

https://doi.org/10.1021/acsomega.3c00074
ACS Omega 2023, 8, 12911−12921

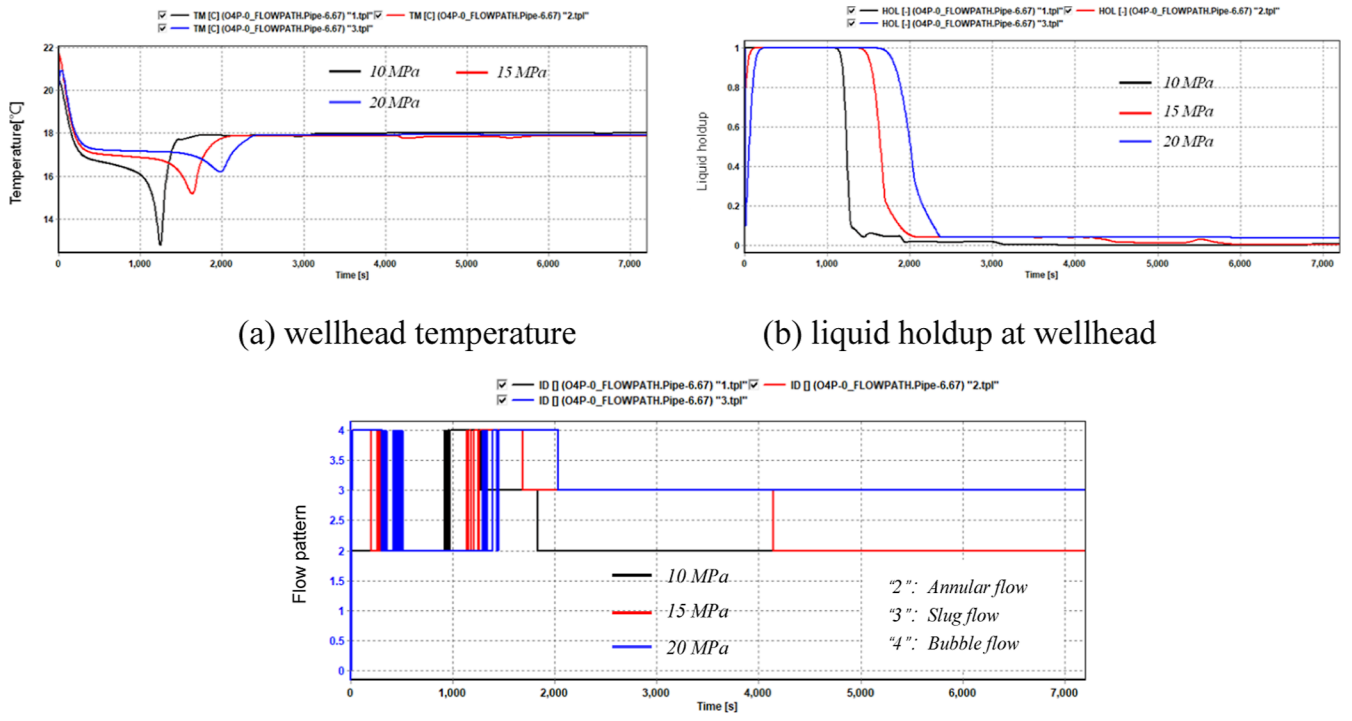

(a) wellhead temperature (b) liquid holdup at wellhead

(c) flow pattern at wellhead

Figure 6. Effect of blowout wellhead pressure on fluid flow in wellbore.

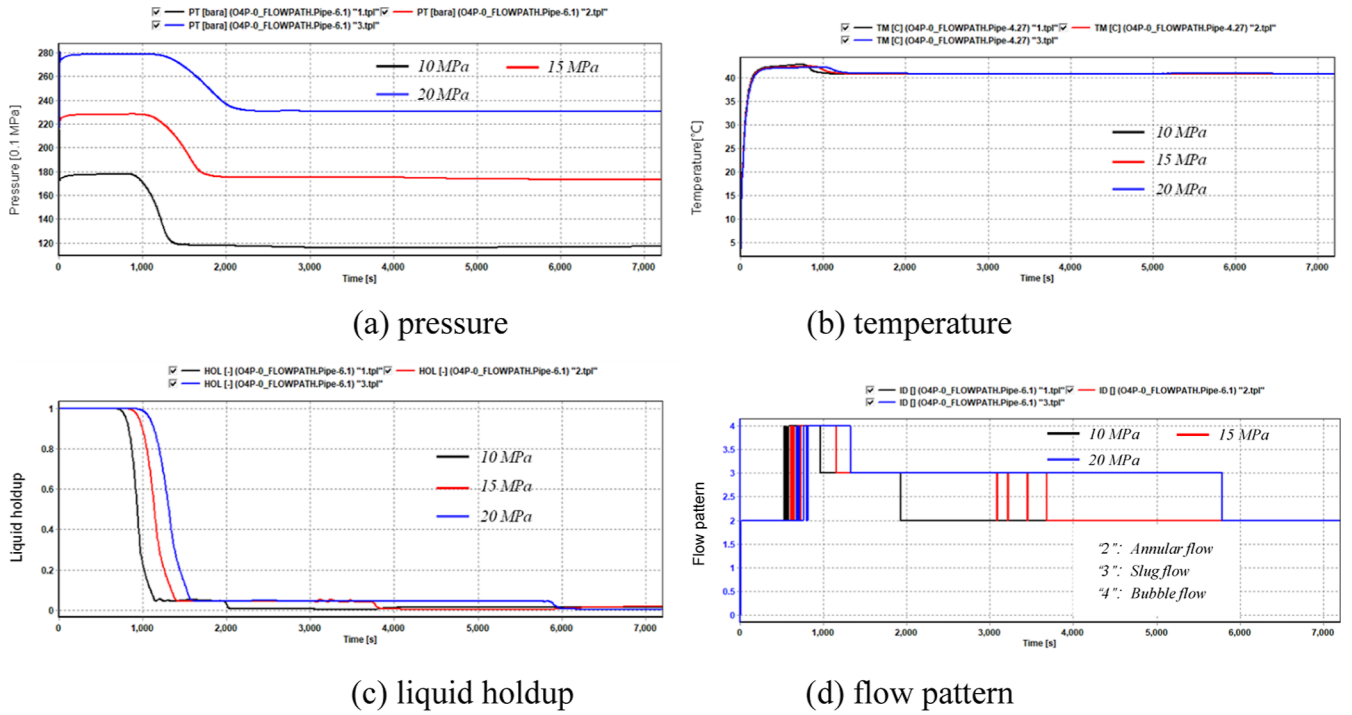

(a) pressure (b) temperature

(c) liquid holdup (d) flow pattern

Figure 7. Pressure, temperature, liquid holdup, and flow pattern at the mud line.

It can be seen from Figure 3c,d that the pressure at the mud line decreases with the discharge of the liquid phase and changes synchronously with the temperature curve. In the initial state, the fluid temperature at the mud line is equal to the sea bottom water temperature (3.2 °C). During blowout, the fluid temperature at the mud line keeps rising, which is caused by the flow of high-temperature liquid at the lower part of the wellbore. When the liquid phase is basically discharged, the fluid in the wellbore is mainly gas phase, and the temperature at the mud line will drop again and gradually become stable.

The change of liquid holdup at the mud line is shown in Figure 4. Comparing the change curve of liquid holdup at the mud line and wellhead, it can be seen that the time when the

https://doi.org/10.1021/acsomega.3c00074
ACS Omega 2023, 8, 12911−12921

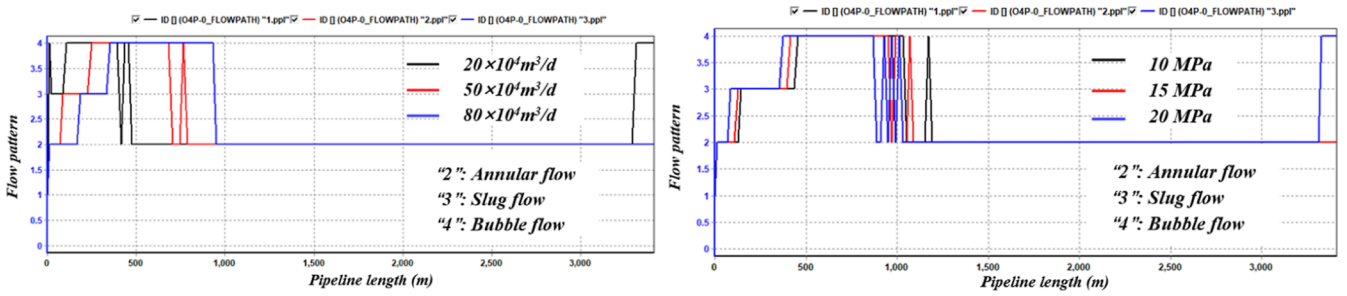

(a) different discharge rates (b) different wellhead pressure

Figure 8. Change of flow pattern along wellbore under different discharge rates and wellhead pressures.

liquid holdup at the mud line drops significantly is slightly earlier than that at the wellhead, and the advance time is about 200−400 s, which indicates that local liquid column sections will be ejected by gas during liquid column discharge.

The flow pattern changes at the wellhead and mud line are shown in Figure 5.

It can be seen from Figure 5a,b that at different times of the same blowout production, bubbly flow patterns will appear at the wellhead and mud line positions in the early stage, and the bubbly flow pattern will change to the slug flow pattern. In the middle and late stages of blowout, the annular flow distribution will prevail. Since the simulation results of OLGA software do not show the foggy flow and agitated flow, the analysis here only involves the bubbly flow, slug flow, and annular flow. In addition, at the same blowout time, taking the blowout 1800 s as an example, the flow pattern at the mud line is different under different blowout output 20×10^4, 50×10^4, and 80×10^4 m^3/d. Bubble flow, slug flow, and annular flow patterns are, respectively, present in the pipe column at the mud line under venting volume.

3.2. Effect of Blowout Wellhead Pressure. In order to reflect the gas expansion effect affected by the pressure reduction in the wellbore, it is assumed that the gas release rate is unchanged (60×10^4 m^3/d). Only the wellhead pressure during blowout will be changed, and the temperature, liquid holdup, and flow pattern changes at the wellhead when the wellhead pressure is 10, 15, and 20 MPa, respectively, are shown in Figure 6.

It can be seen from Figure 6a that the temperature at the wellhead has a similar change feature of decreasing first and then increasing. Since only the wellhead pressure (10, 15, and 20 MPa) at the time of blowout has been changed, the amount of blowout gas has not changed, so the stable value of the wellhead temperature at the later stage of blowout is similar.

From Figure 6b,c, when the amount of blowout gas remains unchanged, the reduction of wellhead blowout pressure will help shorten the blowout duration. Because under the condition of lower pressure in the wellbore, the gas can expand to a larger volume, and the larger gas−liquid ratio makes the liquid column easier to be discharged, which can also be reflected in the flow pattern change diagram. At the same time in the flowback process, slug flow and annular flow are more likely to occur in the wellbore under low wellhead pressure. Bubble flow often appears at the initial stage of flowback under high wellhead pressure, and gradually changes into slug and annular flow patterns in the middle and late stages.

The changes of pressure, temperature, liquid holdup, and flow pattern at the mud line are shown in Figure 7.

It can be seen from Figure 7a that the pressure at the mud line is obviously affected by the wellhead pressure, and the pressure is basically stable in the early stage of flowback. When the liquid column is returned, the pressure drops significantly, and the correlation between the pressure drop value and the wellhead pressure change is not obvious. The pressure at the mud line remains relatively stable in the later stage of blowout. It can be seen from Figure 7b that the change of wellhead pressure has little impact on the temperature value at the mud line, and the temperature at the mud line is basically stable at the same level in the later stage of blowout.

It can be seen from Figure 7c,d that the decline of liquid holdup at the mud line is similar to that at the wellhead. This advance is the time required for the residual liquid to flow from the mud line to the wellhead. The flow pattern change at the mud line is similar to that at the wellhead. Under high wellhead blowout pressure, the bubble flow and slug flow at the mud line last longer, and under low wellhead pressure, the annular flow pattern will appear earlier at the mud line. This is mainly related to the larger gas expansion volume and higher gas−liquid ratio under low pressure.

3.3. Wellbore Flow Pattern Distribution. The flow pattern changes along the well bore under different blowout volumes and blowout wellhead pressuress at 500 s are shown in Figure 8.

It can be seen from Figure 8 that after 500 s of blowout, different flow patterns are distributed along the well bore. Bubble flow and slug flow are mainly present within 1000 m of the lower part of the well bore, and annular flow pattern is mainly present within 1000−3410 m. This is mainly caused by the gradual decrease of the pressure at the upper part of the well bore and the increase of the volume and section gas content of the gas phase during the rising process.

4. RESULTS AND DISCUSSION

The well cleaning process is often accompanied by the formation of hydrate. For example, the size of the blowout rate will also affect the temperature and pressure distribution of the wellbore, thus affecting the formation of hydrate. Therefore, this study establishes a model to predict the risk of hydrate formation during the well cleaning test.

4.1. Distribution of Ambient Temperature outside the Wellbore. The external environment of deep-water gas wells can be divided into stratum section and seawater section from the mud line.[31] In the stratum section from the mud line down to the reservoir, the temperature distribution is

https://doi.org/10.1021/acsomega.3c00074
ACS Omega 2023, 8, 12911−12921

approximately linear, and the temperature change rate can be reflected by the geothermal gradient. In contrast, the temperature distribution regularity of the seawater section above the mud line is poor. The formation and seawater temperature affect the heat transfer characteristics inside and outside the wellbore. Therefore, it is necessary to clarify the environmental temperature distribution characteristics outside the wellbore.

The seawater temperature distribution has a certain correlation with the depth. According to the law of water temperature change, the seawater can be vertically divided into mixed layer, thermocline layer, and thermostatic layer. Among them, the mixing layer is generally within 100 m from the sea level. Under the influence of ocean dynamics and thermal dynamics, the ocean surface and seawater are fully mixed, and the vertical temperature distribution is uniform. The vertical variation of the seawater temperature in the thermocline is more intense, and the temperature gradient is larger, and the water temperature in the thermocline and mixed layer is significantly affected by the sea area and season. The thermostatic layer is in the area with greater seawater depth, the water temperature is maintained at a lower level, the water temperature gradient is small, and it is less affected by the season. Seawater temperature can be calculated by the water temperature fitting formula:[32,33]

In the range with seawater depth less than 200 m:

spring

$$T_w = [T_s(200 - h_w) + 13.68h_w]/200,\ 0 \le h_w < 200\ \text{m} \tag{1}$$

summer

$$T_w = \begin{cases} T_w = T_s,\ 0 \le h_w < 20\ \text{m} \\ [T_s(200 - h_w) + 13.7(h_w - 20)]/180,\ 20 \le h_w < 200\ \text{m} \end{cases} \tag{2}$$

autumn

$$T_w = \begin{cases} T_w = T_s,\ 0 \le h_w < 50\ \text{m} \\ [T_s(200 - h_w) + 13.7(h_w - 50)]/150,\ 50 \le h_w < 200\ \text{m} \end{cases} \tag{3}$$

winter

$$T_w = \begin{cases} T_w = T_s,\ 0 \le h_w < 100\ \text{m} \\ [T_s(200 - h_w) + 13.7(h_w - 100)]/100,\ 100 \le h_w < 200\ \text{m} \end{cases} \tag{4}$$

In the range with seawater depth greater than 200 m

$$T_w = a_2 + (a_1 - a_2)/[1 + \exp(h_w - a_0/a_3)] \tag{5}$$

where T_s is the sea surface temperature, °C; H_w is the seawater depth, m; and a_0, a_1, a_2, and a_3 are empirical coefficients, a_0 = − 130.1, a_1 = 39.4, a_2 = 2.3, and a_3 = 402.7.

Taking deep-water gas well X as an example, the formation depth is 3410 m, the water depth is 1350 m, and the geothermal gradient is 3.87 °C/100 m. Combined with the above water temperature formula, the distribution of external ambient temperature of the wellbore is obtained as shown in Figure 9.

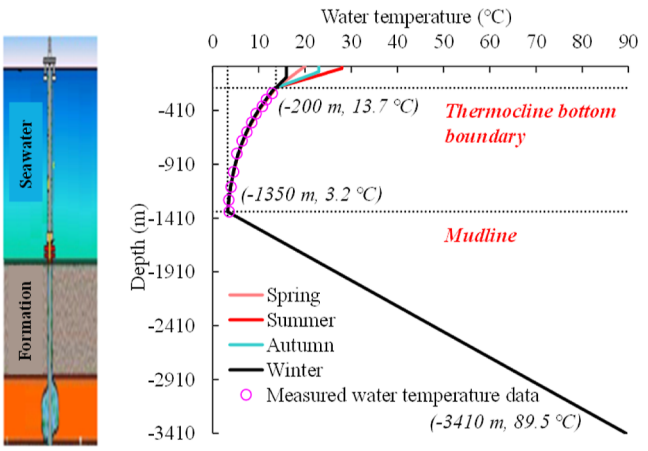

Figure 9. External temperature distribution of deep-water gas well (X Well).

It can be seen from Figure 9 that the external ambient temperature of the well bore decreases first and then increases from the ground to the reservoir. The water temperature of the mixed layer and thermocline within 200 m above the seawater is greatly affected by the surface temperature and season. The water temperature in summer is obviously higher than that in winter. The water temperature at the 1350 m mud line is the lowest point of the temperature along the well bore, reaching 3.2 °C. The formation temperature increases linearly from the mud line to the reservoir, reaching the highest value after reaching the reservoir.

4.2. Hydrate Risk Prediction. *4.2.1. Hydrate Risk Prediction Model.* During the wellbore cleanup process, the mass conservation equation, momentum conservation equation, and energy conservation equation of multiphase flow can be established.[34−38]

1 Mass conservation equation

$$\frac{\partial}{\partial z}(A_c\rho_g v_g E_g) + \frac{\partial}{\partial z}(A_c\rho_p v_p E_p) = 0 \tag{6}$$

where A_c is the test column cross-sectional area, m^2; ρ_g is the density of produced gas, kg/m^3; ρ_p is the density of completion fluid, kg/m^3; E_g is the volume fraction of produced gas, dimensionless; E_p is the volume fraction of completion fluid, dimensionless; v_g is the rising velocity of produced gas, m/s; v_p is the rising velocity of liquid phase, m/s; q_g is the gas production rate, kg/s; and q_p is the liquid production rate, kg/s.

2Momentum conservation equation

$$\frac{dp}{dz} = f_m\frac{\rho_m v_m^2}{2d} + \rho_m v_m\frac{dv_m}{dz} + \rho_m g\cos\alpha \tag{7}$$

where p is the pressure in the tubing, MPa; f_m is the friction coefficient of fluid, dimensionless; and g is the gravity acceleration, m/s^2.

3 Energy conservation equation can be expressed as

https://doi.org/10.1021/acsomega.3c00074
ACS Omega 2023, 8, 12911−12921

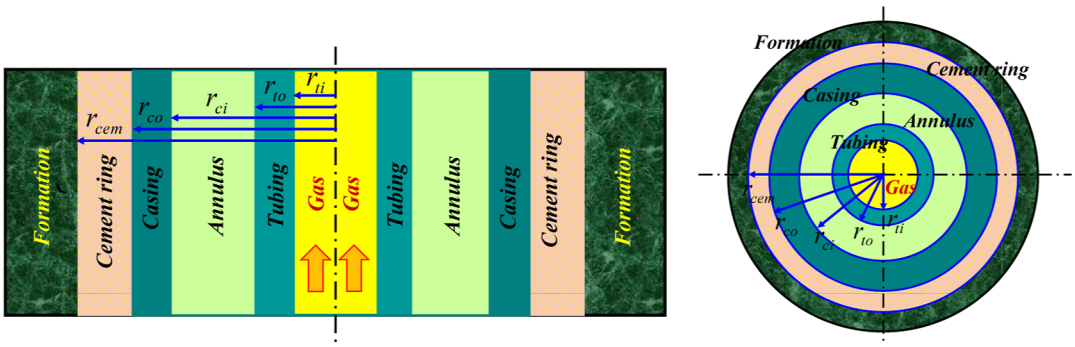

Figure 10. Schematic diagram of the wellbore section below the mud line.

$$\frac{dQ}{dz} = -C_{pm}\frac{dT_f}{dz} + C_{pm}C_{Jm}\frac{dp}{dz} - \frac{v_m dv_m}{dz} - g\sin\alpha - \frac{f_m v_m^2}{2d} \tag{8}$$

where T_f is the temperature in the tubing, K; Q is the heat transfer rate from fluid to the formation or seawater, W; C_{pm} is the specific heat capacity at constant pressure of the mix fluid, J/(kg·K); and C_{Jm} is the Joule−Thomson coefficient of the fluid mixture, dimensionless, and α is the angle of inclination, rad.

Next, take the formation section as an example to introduce the heat transfer characteristics of fluid in the wellbore to the external environment. Below the mud line, natural gas, oil pipe, oil casing ring, casing, cement ring, and formation are distributed from inside to outside. The schematic diagram of wellbore section below mud line is shown in Figure 10.

The heat loss rate of the wellbore can be expressed as

$$\frac{dQ}{dz} = q_m = 2\pi r_{to}U_{ao}(T_m - T_r) \tag{9}$$

where q_m is heat loss rate per unit depth, W/m; T_m is the temperature of fluid in the string, K; T_r is temperature of the outer wall of the cement ring, K; and U_{ao} is the comprehensive thermal conductivity, J/(s·m^2·K).

The heat transfer from the inside of the test string to the formation needs to overcome several thermal resistances, including liquid film thermal resistance, hydrate deposition layer thermal resistance, test string (tubing) thermal resistance, casing thermal resistance, cement ring thermal resistance, annulus radiation, and convection heat transfer resistance. The comprehensive thermal conductivity can be expressed as[39−41]

$$U_{ao} = \left[\frac{r_{to}}{r_{ti}h_f} + \frac{r_{to}}{r_{ti}h_h} + \frac{r_{to}}{\lambda_{tub}}\ln\frac{r_{to}}{r_{ti}} + \frac{1}{h_c + h_r} + \frac{r_{to}}{\lambda_{cas}}\ln\frac{r_{co}}{r_{ci}} + \frac{r_{to}}{\lambda_{cem}}\ln\frac{r_{cem}}{r_{co}}\right]^{-1} \tag{10}$$

Based on the assumption that the formation is unsteady heat conduction, the heat loss rate from the outer wall of cement ring to the formation can be expressed as

$$q_m = \frac{dQ_m}{dz} = 2\pi\lambda_e\left.T_{cem} - T_{ei}\right/f(t) \tag{11}$$

where λ_e is the thermal conductivity of the formation, W/(m·K); T_{ei} is the temperature of the formation, K.

The thermodynamic equations for the formation of gas hydrates can be derived from the thermodynamic equilibrium theory.

$$\frac{\Delta\mu_0}{RT_0} - \int_{T_0}^{T_H}\frac{\Delta H_0 + \Delta C_K(T_H - T_0)}{RT_H^2}dT_H + \int_{p_0}^{p_H}\frac{\Delta V}{RT_H}dp_H = \ln(f_w/f_{wr}) - \sum_{i=1}^{l}M_i\ln\left(1 - \sum_{j=1}^{L}\theta_{ij}\right) \tag{12}$$

$$\ln(f_w/f_{wr}) = \ln x_w \tag{13}$$

If inhibitors exist

$$\ln(f_w/f_{wr}) = \ln y_w x_w \tag{14}$$

More convenient and applicable, the relationship between the shift of hydrate phase equilibrium temperature caused by adding inhibitor and the mass fraction of hydrate inhibitor can be expressed as

$$\Delta T_{eq} = \frac{K_{in}w_{in}}{M_{in}(100 - w_{in})} \tag{15}$$

where M_{in} is the relative molar mass of inhibitor, g/mol; W_{in} is the mass fraction of inhibitor solution; and K_{in} is the mass transfer coefficient related to the inhibitor type. For methanol, isopropanol, and ammonia, K_{in} = 1228, for calcium chloride, K_{in} = 1200, and for diethylene glycol, K_{in} = 24250.

According to the above method, the hydrate formation risk characteristics under different test conditions can be obtained by changing the given parameters.

4.2.2. Prediction Result. In order to discuss the influence of test conditions on hydrate formation, the regional distribution laws of hydrate formation under different test gas volumes, different production liquid gas ratios, and different methanol inhibitor injection volumes were analyzed.

1 Test gas volume

At a constant liquid gas ratio (10 m^3/10^{4}m^3), the test gas volumes are 20 × 10^4 m^3/d, 40 × 10^4 m^3/d, 60 10^4 m^3/d, 80 × 10^4 m^3/d, and 100 × 10^4 m^3/d. The distribution of wellbore temperature field and hydrate generation area are shown in Figure 11.

It can be seen from Figure 11 that with the increase of test gas volume, the fluid temperature distribution curve gradually moves to the right, and the internal temperature of the wellbore gradually increases. This is because the fluid in the wellbore carries more heat under high gas production, the flow temperature is less affected by the external low temperature environment, and the temperature changes more gently. When

https://doi.org/10.1021/acsomega.3c00074
ACS Omega 2023, 8, 12911−12921

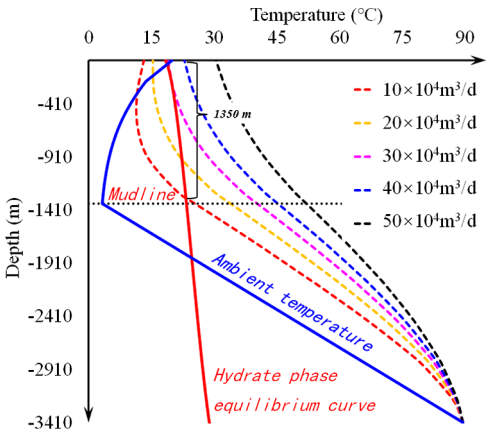

Figure 11. Distribution of hydrate formation area under different test gas volumes.

the temperature distribution curve intersects the hydrate phase equilibrium curve, the closed area on the left side of the phase equilibrium generated by the intersection is the hydrate generation area. It can be seen that when the gas production is 10×10^4 m^3/d, the hydrate generation area in the wellbore is 1350 m, and when the gas production is higher than 30×10^4 m^3/d, the temperature curve and hydrate phase equilibrium curve no longer intersect, and the hydrate formation area disappears.

(2) Production liquid gas ratio

At constant test yield (20×10^4 m^3/d), the distribution of wellbore temperature field and hydrate generation area at the liquid gas ratios of 0, 15 , 30, 45, and 60 $m^3/10^4m^3$ is shown in Figure 12.

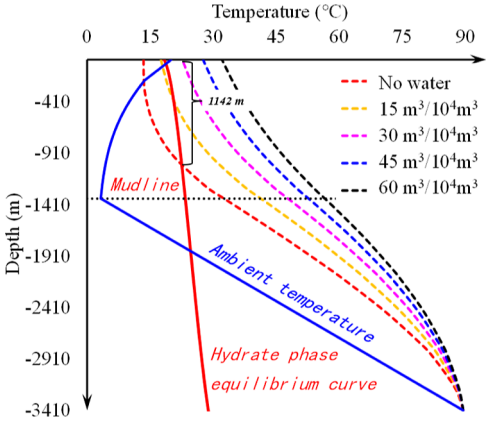

Figure 12. Distribution of hydrate formation area under different liquid−gas ratios.

It can be seen from Figure 12 that when the test gas volume is constant, the temperature distribution in the wellbore increases with the increase of the liquid gas ratio because the heat capacity of the water phase is far greater than that of the gas phase, which can store more heat and slow down the heat loss rate. It can be seen that when the gas production is 20×10^4 m^3/d, when the liquid gas ratio increases from 0 to 15 $m^3/10^4m^3$, the temperature at the wellhead increases from 13.4 to 17.6 °C. In addition, when there is no water production, the length of the area meeting hydrate generation in the wellbore is 1142 m. When the liquid gas ratio is 30 $m^3/10^4m^3$, there is no hydrate generation area in the wellbore, and the critical liquid gas ratio of the area without hydrate generation is 18 $m^3/10^4m^3$. It can be seen that when the water yield or liquid gas ratio increases to a certain value, the wellbore temperature rise caused by the water yield can significantly shorten the hydrate generation area and reduce the risk of hydrate deposition. When the water yield or liquid gas ratio is lower than the critical value, the increase of water yield will increase the risk of hydrate deposition due to the increase of hydrate generation and deposition.

3 Methanol inhibitor injection volume

At constant test gas volume (20×10^4 m^3/d) and liquid gas ratio (10 $m^3/10^4m^3$), the wellbore temperature field and hydrate generation area distribution under different methanol consumption (0, 7, 14, 20, and 25 wt %) are shown in Figure 13.

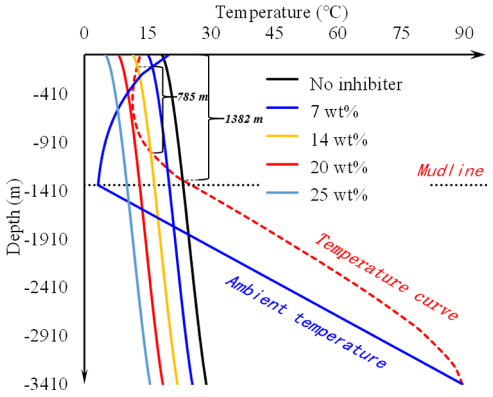

Figure 13. Distribution of hydrate formation area under different methanol contents.

As shown in Figure 13, when the methane content changes, the wellbore temperature distribution curve basically does not change, while the hydrate phase equilibrium curve changes. It can be seen that the methanol content has little effect on the wellbore temperature distribution, but it will affect the hydrate formation conditions, and affect the distribution of hydrate formation areas in the wellbore. When the methanol content increases, the hydrate phase equilibrium curve gradually moves to the left, and the difficulty of hydrate formation increases. Under the above test conditions, without methanol inhibitor, the hydrate formation area in the wellbore is 1382 m. When the methanol mass fraction is 14%, the hydrate formation area is shortened to 785 m, while when the methanol content increases to 20 wt %, the hydrate formation area disappears.

5. CONCLUSIONS

1In the process of deep-water gas well cleanup, the initial temperature at the wellhead is equal to the sea level temperature, which decreases first, then increases, and finally tends to be flat. The flow temperature at the mud line first increases, then decreases, and then flattens.

2 The liquid holdup in the wellbore gradually decreases from ″1″ to ″0″, indicating that the liquid phase in the wellbore is basically drained, and the residual liquid phase in the later period comes from the formation produced water or gas condensate water. During liquid column discharge, local liquid column will be ejected by gas.

https://doi.org/10.1021/acsomega.3c00074
ACS Omega 2023, 8, 12911−12921

3The reduction of wellhead blowout pressure will help shorten the blowout duration, and the gas will expand to a larger volume. Slug flow and annular flow are more likely to occur in the wellbore under low wellhead pressure. Bubble flow often appears at the initial stage of flowback under high wellhead pressure and gradually changes to slug and annular flow patterns in the middle and late stages;

4 At the same time of blowout, the well bore will also show different flow pattern distributions along the way. Bubble flow and slug flow are often present at the lower part of the wellbore, and the annular flow pattern is dominant in the upper and middle part of the wellbore.

5 The prediction method of hydrate formation area proposed in this study is based on the coupled calculation model of temperature and pressure and the hydrate phase equilibrium model, which is applicable to the study of hydrate risk in the process of deep-water gas well cleaning and blowout.

6 As for high liquid−gas ratio condition, properly speeding up the well cleanup process and using hydrate inhibitors can effectively reduce the hydrate risk in the process of deep-water gas well cleanup.

■ ETHICAL STATEMENT

On behalf of all the co-authors, the corresponding author states that there are no ethical statements contained in the paper.

■ AUTHOR INFORMATION

Corresponding Author

Zheng Sun − *State Key Laboratory of Coal Resources and Safe Mining, China University of Mining and Technology, Xuzhou 221116, China; School of Mining, China University of Mining and Technology, Xuzhou 221116, China;* orcid.org/0000-0002-3844-3953; Phone: +86-18500610758; Email: szcup613@163.com

Author

Dayong Chen − *State Key Laboratory of Coal Resources and Safe Mining, China University of Mining and Technology, Xuzhou 221116, China; School of Mining, China University of Mining and Technology, Xuzhou 221116, China*

Complete contact information is available at: https://pubs.acs.org/10.1021/acsomega.3c00074

Notes

The authors declare no competing financial interest.

■ ACKNOWLEDGMENTS

The authors acknowledge the financial support from National Natural Science Foundation Projects of China (no. 51604261 and no. 52104099) and Natural Science Foundation Projects of Jiangsu Province (no. BK20210508). We also acknowledge China University of Mining & Technology for the permission to publish this work.

■ REFERENCES

(1) Pettingill, H. S.; Weimer, P. Worlwide deepwater exploration and production: past, present, and future. *Leading Edge* **2002**, *21*, 371−376.

(2) Kabir, C. S.; Yi, X.; Jakymec, M.; Hasan, A. R. Interpreting distributed-temperature measurements in deepwater gas-well testing: estimation of static and dynamic thermal gradients and flow rates. *SPE Prod. Oper.* **2014**, *29*, 97−104.

(3) Stomp, R. J.; Fraser, G. J.; Actis, S. C.; Eaton, L. F.; Freedman, K. C. *Deepwater DST planning and operations from a DP vessel*; SPE Annual Technical Conference and Exhibition, 2004. .

(4) Gao, Y.; Chen, Y.; Wang, Z.; Chen, L.; Zhao, X.; Sun, B. Experimental study on heat transfer in hydrate-bearing reservoirs during drilling processes. *Ocean Engineering* **2019**, *183*, 262−269.

(5) Gao, Y.; Cui, Y.; Xu, B.; Sun, B.; Zhao, X.; Li, H.; Chen, L. Two phase flow heat transfer analysis at different flow patterns in the wellbore. *Applied thermal engineering* **2017**, *117*, 544−552.

(6) Fu, B.; Neff, S.; Mathur, A.; Bakeev, K. Application of low-dosage hydrate inhibitors in deepwater operations. *SPE Prod. Facil.* **2002**, *17*, 133−137.

(7) Aman, Z. M.; Aspenes, G.; Sloan, E. D.; Sum, A. K.; Koh, C. A. *The Effect of Chemistry and System Conditions on Hydrate Interparticle Adhesion Forces Toward Aggregation and Hydrate Plug Formation*; SPE International Symposium on Oilfield Chemistry 2011.

(8) Chaudhari, P.; Zerpa, L. E.; Sum, A. K. A correlation to quantify hydrate plugging risk in oil and gas production pipelines based on hydrate transportability parameters. *Journal of Natural Gas Science and Engineering* **2018**, *58*, 152−161.

(9) Rashid, M.; Luo, M.; Ashraf, U.; Hussain, W.; Ali, N.; Rahman, N.; Hussain, S.; Aleksandrovich Martyushev, D.; Vo Thanh, H.; Anees, A. Reservoir Quality Prediction of Gas-Bearing Carbonate Sediments in the Qadirpur Field: Insights from Advanced Machine Learning Approaches of SOM and Cluster Analysis. *Minerals* **2022**, *13*, 29.

(10) Sun, Z.; Wang, S.; Xiong, H.; Wu, K.; Shi, J. Optimal nanocone geometry for water flow. *AIChE J.* **2022**, *68*, No. e17543.

(11) Van der Waals, J. H.; Platteeuw, J. C. *Clathrate solutions*, 1959.

(12) Parrish, W. R.; Prausnitz, J. M. Dissociation pressures of gas hydrates formed by gas mixtures. *Industrial & Engineering Chemistry Process Design and Development* **1972**, *11*, 26−35.

(13) Ng, H. J.; Robinson, D. B. The measurement and prediction of hydrate formation in liquid hydrocarbon-water systems. *Ind. Eng. Chem. Fundam.* **1976**, *15*, 293−298.

(14) John, V. T.; Papadopoulos, K. D.; Holder, G. D. A generalized model for predicting equilibrium conditions for gas hydrates. *AIChE J.* **1985**, *31*, 252−259.

(15) Chen, G. J.; Guo, T. M. A new approach to gas hydrate modelling. *Chem. Eng. J.* **1998**, *71*, 145−151.

(16) Chen, G. J.; Guo, T. M. Thermodynamic modeling of hydrate formation based on new concepts. *Fluid Phase Equilib.* **1996**, *122*, 43−65.

(17) Zakharov, L. A.; Martyushev, D. A.; Ponomareva, I. N. Predicting dynamic formation pressure using artificial intelligence methods. *Journal of Mining Institute* **2022**, *253*, 23−32.

(18) Sun, Z.; Li, X.; Liu, W.; Zhang, T.; He, M.; Nasrabadi, H. Molecular Dynamics of Methane Flow Behavior through Realistic Organic Nanopores under Geologic Shale Condition: Pore size and Kerogen Types. *Chem. Eng. J.* **2020**, *398*, 124341.

(19) Javanmardi, J.; Moshfeghian, M. A new approach for prediction of gas hydrate formation conditions in aqueous electrolyte solutions. *Fluid Phase Equilib.* **2000**, *168*, 135−148.

(20) Reyna, E. M.; Stewart, S. R. *Case History of the Removal of a Hydrate Plug Formed During Deep Water Well Testing*; SPE/IADC Drilling Conference: Amsterdam, 2001.

(21) Arrieta, V. V.; Torralba, A. O.; Hernandez, P. C.; García, E. R.; Maia, C. T.; Guajardo, M. Case History: Lessons learned From Retrieval of Coiled Tubing Stuck by Massive Hydrate Plug When Well Testing in an Ultra Deep-Water Gas Well in Mexico. *SPE Prod. Oper.* **2011**, *26*, 337−342.

(22) Wang, Z.; Yu, J.; Zhang, J.; Liu, S.; Gao, Y.; Xiang, H.; Sun, B. Improved thermal model considering hydrate formation and deposition in gas-dominated systems with free water. *Fuel* **2019**, *236*, 870−879.

(23) Wang, Z.; Zhao, Y.; Zhang, J.; Pan, S.; Yu, J.; Sun, B. Flow assurance during deep-water gas well testing: Hydrate blockage prediction and prevention. *J. Petrol. Sci. Eng.* **2018**, *163*, 211−216.
(24) Liu, W.; Hu, J.; Li, X.; Sun, F.; Sun, Z.; Zhou, Y. Research on evaluation method of wellbore hydrate blocking degree during deep-water gas well testing. *J. Nat. Gas Sci. Eng.* **2018**, *59*, 168−182.
(25) Fu, W.; Wang, Z.; Sun, B.; Ji, C.; Zhang, J. Multiple controlling factors for methane hydrate formation in water-continuous system. *Int. J. Heat Mass Transf.* **2019**, *131*, 757−771.
(26) Zhang, J.; Wang, Z.; Liu, S.; Zhang, W.; Yu, J.; Sun, B. Prediction of hydrate deposition in pipelines to improve gas transportation efficiency and safety. *Applied Energy* **2019**, *253*, 113521.
(27) Zhang, J.; Wang, Z.; Sun, B.; Sun, X.; Liao, Y. An integrated prediction model of hydrate blockage formation in deep-water gas wells. *Int. J. Heat Mass Transf.* **2019**, *140*, 187−202.
(28) Ponomareva, I. N.; Martyushev, D. A.; Govindarajan, S. K. *A new approach to predict the formation pressure using multiple regression analysis: Case study from Sukharev oil field reservoir − Russia*; Journal of King University − Engineering Sciences, 2022.
(29) Sun, Z.; Huang, B.; Liu, Y.; Jiang, Y.; Zhang, Z.; Hou, M.; Li, Y. Gas-phase production equation for CBM reservoirs: Interaction between hydraulic fracturing and coal orthotropic feature. *Journal of Petroleum Science and Engineering* **2022**, *213*, 110428.
(30) Ponomareva, I. N.; Galkin, V. I.; Martyushev, D. A. Operational method for determining bottom hole pressure in mechanized oil producing wells, based on the application of multivariate regression analysis. *Petroleum Research* **2021**, *6*, 351−360.
(31) Yu, P.; Dempsey, D.; Rinaldi, A. P.; Calibugan, A.; Ritz, V. A.; Archer, R. Association between Injection and Microseismicity in Geothermal Fields with Multiple Wells: Data-driven Modelling of Rotokawa, New Zealand, and Húsmúli, Iceland. *J. Geophys. Res.: Solid Earth* **2023**, No. e2022JB025952.
(32) Hasan, A. R.; Kabir, C. S.; Lin, D. Analytic wellbore temperature model for transient gas-well testing. *SPE J* **2005**, *8*, 240−247.
(33) Levitus, S.; Boyer, T. *World Ocean Atlas 1994, 4: Temperature. Wash., D. C. NOAA Atlas NESDIS 4*; U. S. Gov. Printing Office, 1994, p 117.
(34) Dong, X.; Liu, H.; Pang, Z.; Wang, C.; Lu, C. Flow and heat transfer characteristics of multi-thermal fluid in a dual-string horizontal well. *Numerical Heat Transfer, Part A: Applications* **2014**, *66*, 185−204.
(35) Shijun, H. U.; Qiu, L.; Linsong, C. H.; Guojin, Z.; Meng, Z. An evaluation model on along-pipe thermal parameter of multi-component heat fluid injected in offshore reservoirs. *Journal of Southwest Petroleum University (Science & Technology Edition)* **2015**, *37*, 91−95.
(36) Coulter, D. M.; Bardon, M. F. Revised equation improves flowing gas temperature prediction. *Oil Gas J.* **1979**, *77*, 107−108.
(37) Shiu, K. C.; Beggs, H. D. Predicting temperatures in flowing oil wells. *Journal of Energy Resources Technology* **1980**, *102*, 2−11.
(38) Ali, S. M. F. A comprehensive wellbore stream/water flow model for steam injection and geothermal applications. *SPE J* **1981**, *21*, 527−534.
(39) Lin, R.; Shao, C.; Li, J. Study on two-phase flow and heat transfer in offshore wells. *J. Pet. Sci. Eng.* **2013**, *111*, 42−49.
(40) Sun, B. J.; Gao, Y. H.; Ma, Y. Q.; Wang, Z. Y.; Li, H. Research on the heat transfer law of gas-liquid two-phase flow in a deep-water wellbore. *WIT Transactions on Engineering Sciences* **2012**, *74*, 465−479.
(41) Galkin, V. I.; Martyushev, D. A.; Ponomareva, I. N.; Chernykh, I. A. Developing features of the near-bottomhole zones in productive formations at fields with high gas saturation of formation oil. *Journal of Mining Institute* **2021**, *249*, 386−392.

https://doi.org/10.1021/acsomega.3c00074
ACS Omega 2023, 8, 12911−12921